AGU PUBLICATIONS

JGR

Journal of Geophysical Research: Solid Earth

RESEARCH ARTICLE
10.1002/2017JB014379

Key Points:
- We significantly reduce correlated error in GRACE data over Greenland using an extended empirical orthogonal function filter
- Winter month-to-month ice mass changes in Greenland agree well with surface mass balance derived from a regional climate model, RACMO2.3/GR
- We estimate the spatial distribution of monthly mass evolutions in Greenland from GRACE solutions

Supporting Information:
- Supporting Information S1

Correspondence to:
K.-W. Seo,
seokiweon@snu.ac.kr

Citation:
Eom, J., K.-W. Seo, C.-K. Lee, and C. R. Wilson (2017), Correlated error reduction in GRACE data over Greenland using extended empirical orthogonal functions, *J. Geophys. Res. Solid Earth*, *122*, 5578–5590, doi:10.1002/2017JB014379.

Received 10 JAN 2017
Accepted 11 JUN 2017
Accepted article online 13 JUN 2017
Published online 3 JUL 2017

Correlated error reduction in GRACE data over Greenland using extended empirical orthogonal functions

Jooyoung Eom[1], Ki-Weon Seo[2], Choon-Ki Lee[1], and C. R. Wilson[3]

[1]Unit of Ice Sheet and Sea Level Changes, Korea Polar Research Institute, Incheon, South Korea, [2]Department of Earth Science and Education, Seoul National University, Seoul, South Korea, [3]Department of Geological Sciences, Jackson School of Geosciences, University of Texas at Austin, Austin, Texas, USA

Abstract Surface mass change estimates from Gravity Recovery and Climate Experiment (GRACE) spherical harmonic solutions are contaminated by north-south stripe noise due largely to aliasing of high-frequency variations into monthly samples. These meridional stripes are especially troubling for ice mass balance studies of the Greenland Ice Sheet (GrIS) where large ice mass variations are known to occur along north-south trending coastlines. By assuming that mass variations and noise have different patterns in both space and time over Greenland, we use extended empirical orthogonal functions (EEOFs) to filter out this noise. The method is compared with a conventional approach, by examining both continent-wide estimates and regional changes. GRACE results are compared with independent regional estimates derived from a climate model. The EEOF filter is effective at separating ice mass change signals from meridional stripe noise, with better rejection of high temporal frequency noise and less signal attenuation and spatial smoothing compared to a conventional method. We use EEOF-filtered GRACE data to examine regional seasonal variations. Consistent with surface and other data, results show ice mass loss along the west, southwest, and east coasts during summer and gain in these regions during winter. In addition, there is summer ice mass gain in the central region of the GrIS.

1. Introduction

The Greenland Ice Sheet (GrIS) is one of the most important contributors to global mean sea level rise [*Vaughan et al.*, 2013], with an estimated ice mass loss of 250 Gt/yr, equivalent to sea level rise of 0.69 mm/yr, more than from Antarctica (0.50 mm/yr) or mountain glaciers (0.54 mm/yr) [*Chen et al.*, 2013]. While some GrIS loss estimates have used remote sensing observations (airborne and spaceborne radar and laser altimetry surface elevation change [*Zwally et al.*, 2011] and satellite interferometric synthetic aperture radar ice velocity measurements [*Rignot and Mouginot*, 2012]), these require assumed values for additional parameters such as ice thickness or density [*Khan et al.*, 2015]. In contrast, the Gravity Recovery and Climate Experiment (GRACE) has provided direct estimates of mass changes over the GrIS since its launch in 2002. Recent GRACE estimates show significant GrIS mass loss, at rates ranging from 249 Gt/yr to 280 Gt/yr and acceleration of loss in the range 21 Gt/yr^2 to 31 Gt/yr^2 [*Rignot et al.*, 2011; *Schrama et al.*, 2014; *Velicogna and Wahr*, 2013; *Wouters et al.*, 2013].

In addition to long-term losses, GrIS mass also varies month to month [*Wouters et al.*, 2008], in response to surface mass balance (SMB) processes. Both precipitation and meltwater runoff [*van den Broeke et al.*, 2009] are important, but another contributor is varying ice discharge rates at marine-terminating glaciers. Seasonal variations in discharge rates have been associated with meltwater penetration to the subglacial hydrologic system [*Moon et al.*, 2014]. GRACE estimates at these shorter periods are difficult in the presence of noise in GRACE data, especially meridional stripes in spherical harmonic (SH) solutions. *Swenson and Wahr* [2006] found these stripes to be associated with correlated variations of SH coefficients and developed a decorrelation filter to suppress them. It has been recognized that the filter may also remove signal or possibly introduce noise [*Velicogna and Wahr*, 2013]. This could be a problem for GrIS estimates due to the north-south orientation of recognized signals along Greenland's coastlines.

Another filtering approach, based upon empirical orthogonal functions (EOFs), also known as principal component analysis or singular spectrum analysis (SSA), has been applied to GRACE data previously [*Chambers*, 2006; *Forootan and Kusche*, 2012; *Frappart et al.*, 2010; *Schmeer et al.*, 2012; *Schrama and Wouters*, 2011; *Vianna et al.*, 2007]. This technique decomposes the data into different modes consisting of spatial patterns and associated temporal variations. *Wouters and Schrama* [2007] used EOFs to distinguish signal and noise. Although this was largely successful, additional spatial smoothing was necessary to suppress residual errors. Because the EOF method is purely empirical, both spatially correlated signal and noise may be incorporated into the same mode. For this reason, the EOF method would not be effective in separating GrIS signal from noise where spatial patterns of signal and noise are similar. This limitation also applies to other decorrelation methods that depend upon spatial characteristics of GRACE time-varying solutions in a given month [e.g., *Kusche*, 2007].

The EOF method can be extended to include correlations over time, which would allow signal and noise to be separable if the two have distinct temporal variations. Ice mass signals are expected to change slowly at time scales ranging from secular to subseasonal, while noise should be dominant at shorter periods. This motivates development of a modified EOF filtering method that considers spatial and temporal correlations simultaneously. As shown below, the approach is successful in obtaining month-to-month GrIS mass change from GRACE with little signal attenuation and effective suppression of noise.

2. Data and Methods

2.1. Monthly GRACE Solutions

GRACE RL05 solutions (Center for Space Research (CSR), University of Texas at Austin) are used in this study. These provide geoid heights from monthly SH coefficients at degrees and orders up to 60. We use 132 monthly solutions from January 2003 to August 2014. After linearly interpolating SH coefficients for missing months (June 2003; January and June 2011; May and October 2012; and March, August, and September 2013), there are 140 monthly solutions. Interpolation is needed because EOF decomposition, described in the following section, is best done with uniform temporal sampling. Degree 1 coefficients are estimated using an ocean model and GRACE data [*Swenson et al.*, 2008]. Degree 2 zonal harmonic (C20) coefficients are replaced with satellite laser ranging values [*Cheng and Tapley*, 2004]. Postglacial rebound (PGR), Earth's viscoelastic responses from past ice loading, is removed using the ICE-5G model [*A et al.*, 2013]. We remove means of resulting SH coefficients from each monthly solution and express results in units of surface mass change [*Wahr et al.*, 1998]. Changes from month to month should largely be due to surface ice and water redistribution plus contamination from alias errors and random noise.

2.2. Localization of GRACE Coefficients

Previous GRACE studies using EOFs decomposed global SHs to separate signal and noise [*Schrama et al.*, 2007; *Wouters and Schrama*, 2007; *Boergens et al.*, 2014] and were successful when globally coherent signal was discernable from noise. However, as noted above, GrIS ice mass signals in coastal areas have a spatial pattern similar to meridional stripe noise. As a result, the conventional EOF approach is unlikely to be optimum for the GrIS.

As first step in examining the GrIS, we localize GRACE SHs to Greenland. *Slepian* [1983] showed how to develop a basis of orthogonal functions to maximize energy of time series in a limited time interval or frequency band, and the Slepian method was adapted by *Wieczorek and Simons* [2005] to a sphere. Slepian basis functions that concentrate global SHs to the Greenland region were constructed up to degree 60, the maximum in GRACE data. The region of concentration included a buffer zone of 0.5° extending into the oceans around Greenland, to account for possible leakage in coastal areas [*Harig and Simons*, 2012]. These new Slepian basis functions are linear combinations of the global SHs.

2.3. Extended EOF

The extended EOF (EEOF) method was initially developed to identify propagating waves in spatiotemporal data sets [*Weare and Nasstrom*, 1982], unlike the original EOF approach which looks for spatially correlated modes. Because EEOF methods have been presented in many references [e.g., *Hannachi et al.*, 2007; *Navarra and Simoncini*, 2010; *Tangang et al.*, 1998; *von Storch and Navarra*, 1999], only a very concise summary is presented here. The EEOF approach is similar to conventional EOF but differs in the structure of the data matrix before and after decomposition. To clarify this difference, consider spatiotemporal data, with numbers of spatial and temporal samples p and n, respectively. For GRACE, n = 140, the number of months, and p is the number of SH coefficients. Each time-varying SH coefficient of a certain degree and order is a column vector, $\boldsymbol{d}_j^{(1,n)} = \left(d_j^1, d_j^2, \cdots, d_j^i, \cdots, d_j^n\right)^T$, where j is the index from 1 to p. The superscript indicates an element of a column vector for the ith month. In conventional EOF analysis, coefficients are arranged in an $n \times p$ matrix, $\boldsymbol{D} = \left[\boldsymbol{d}_1^{(1,n)}\ \boldsymbol{d}_2^{(1,n)} \cdots \boldsymbol{d}_p^{(1,n)}\right]$. In the EEOF method, column vectors $\boldsymbol{d}_j^{(1,n)}$ are successively time lagged using a window length parameter M. The lagged versions are arranged in an extended submatrix $\boldsymbol{D}_j^E$. For example, $\boldsymbol{d}_1^{(1,n)}$ is extended to become

$$\boldsymbol{D}_1^E = \left[\boldsymbol{d}_1^{(1,n-M+1)}\ \boldsymbol{d}_1^{(2,n-M+2)} \cdots \boldsymbol{d}_1^{(M,n)}\right] \tag{1}$$

The full extended data matrix $\boldsymbol{D}^E$ is given by

$$\boldsymbol{D}^E = \left[\boldsymbol{D}_1^E\ \boldsymbol{D}_2^E \cdots \boldsymbol{D}_p^E\right] \tag{2}$$

M is set by the temporal scale of interest. For example, $M = 12$ would be suitable for investigating spatial patterns in monthly data correlated at annual or shorter time scales. The particular choice $M = 5$ used in this study is discussed below.

In conventional EOF analysis, spatial patterns and associated time series of data set ($\boldsymbol{D}$) are separated into EOFs via the singular value decomposition (SVD):

$$\boldsymbol{D} = \boldsymbol{U}\Sigma\boldsymbol{V}^{\mathrm{T}} \tag{3}$$

where $\boldsymbol{V}$ and $\boldsymbol{U}$ are orthogonal matrices, with column vectors representing spatial patterns and associated time variability, respectively. $\boldsymbol{\Sigma}$ is a rectangular diagonal matrix containing singular values of $\boldsymbol{D}$, which measure the explained variance of each mode (spatial pattern and associated temporal variation). In the EEOF method, SVD decomposition of the extended data matrix, $\boldsymbol{D}^E$ yields elements in $\boldsymbol{V}$ that include time-lagged variations up to M months:

$$\boldsymbol{V} = \begin{bmatrix} v_1^1(1) & v_1^1(2) & \cdots & v_1^1(M) & v_1^2(1) & \cdots & v_1^j(t) & \cdots & v_1^p(M) \\ \vdots & \vdots & \ddots & \vdots & \vdots & \ddots & \vdots & \ddots & \vdots \\ v_k^1(1) & v_k^1(2) & \cdots & v_k^1(M) & v_k^2(1) & \cdots & v_k^j(t) & \cdots & v_k^p(M) \\ \vdots & \vdots & \ddots & \vdots & \vdots & \ddots & \vdots & \ddots & \vdots \end{bmatrix}^T, \tag{4}$$

where subscript and superscript indicate kth spatial mode and jth location index, respectively, and t in parentheses is a positive integer related to the window length parameter ranging from 1 to M. Therefore, the kth column of $\boldsymbol{V}$ represents the kth spatial mode and is rearranged for simplicity as follows:

$$\boldsymbol{V}_k = \left[\boldsymbol{v}_k^{(1,p)}(1)\ \boldsymbol{v}_k^{(1,p)}(2) \ldots \boldsymbol{v}_k^{(1,p)}(M)\right], \tag{5}$$

where $\boldsymbol{v}_k^{(1,p)}(t) = \left(v_k^1(t), v_k^2(t), \cdots, v_k^j(t), \cdots, v_k^p(t)\right)^{\mathrm{T}}$.

The conventional EOF method can be used to filter a given data set by retaining only desired modes, and the reconstructed (filtered) data set, $\boldsymbol{D}^{'}$, can be described as

$$\boldsymbol{D}^{'} = \sum_{k=1}^{N} \chi_k \sigma_k \boldsymbol{u}_k \boldsymbol{v}_k^T, \qquad \text{where } N = \min(n, p), \tag{6}$$

where $\boldsymbol{u_k}$ and $\boldsymbol{v_k}$ are th column vectors of $\boldsymbol{U}$ and $\boldsymbol{V}$, respectively, and σ_k is the kth diagonal element of $\boldsymbol{\Sigma}$ in equation (3). The χ_k is a weighting parameter to determine which column vectors are included in the reconstruction. For example, if the first and third modes are retained, χ_1 and χ_3 are ones while others are zeros. If all χ_k are ones, the reconstructed $\boldsymbol{D}^{'}$ is identical to initial data set, $\boldsymbol{D}$.

In the EEOF method, reconstruction differs because modes also include spatiotemporal variation as shown in equation (4). The EEOF reconstruction formula is

$$\boldsymbol{D}^{'} = \boldsymbol{M} \sum_{k=1}^{N} \chi_k \sigma_k \boldsymbol{u}_k * \boldsymbol{V}_k^T, \qquad \text{where } N = \min(m - M + 1, Mp), \tag{7}$$

where $\boldsymbol{u}_k$ is kth column vector of $\boldsymbol{U}$ in equation (3) with length of $(n-M+1)$. The asterisk is a convolution operator converting the prevector (i.e., $\boldsymbol{u}_k$) to a Toeplitz matrix, enabling multiplication with the following matrix:

$$\boldsymbol{u}_k{}^*\boldsymbol{A} = \begin{bmatrix} u_k^1 & 0 & \cdots & 0 \\ u_k^2 & u_k^1 & \cdots & \vdots \\ u_k^3 & u_k^2 & \cdots & \vdots \\ \vdots & \vdots & \ddots & \vdots \\ 0 & 0 & \cdots & u_k^{m-M+1} \end{bmatrix} \boldsymbol{A}. \tag{8}$$

$\boldsymbol{M}$ in equation (7) is a diagonal $n \times n$ weighting matrix. Because the extended data matrix, $\boldsymbol{D}^E$, has fewer terms at smaller lags, values of M are chosen as follows:

$$\boldsymbol{M} = \operatorname{diag}\left(1, \frac{1}{2}, \cdots, \frac{1}{M-1}, \frac{1}{M}, \cdots, \frac{1}{M}, \frac{1}{M-1}, \cdots, \frac{1}{2}, 1\right). \tag{9}$$

The EEOF method, and related multichannel singular spectrum analysis (MSSA), use temporally lagged correlations [*Hannachi et al.*, 2007], to distinguish low-frequency variability (in this case presumably ice mass signal) from higher-frequency variability (presumably noise). Although the two methods are mathematically equivalent, there is a difference in their application. MSSA aims to identify known or unknown periodic signals in the presence of noise [e.g., *Ghil et al.*, 2002; *Rangelova et al.*, 2009, 2012; *Zotov et al.*, 2015, 2016]. To do this, MSSA incorporates a large number of lags M, which leads to increased repetition of signals of interest and improved statistical confidence in estimated signals [*Ghil et al.*, 2002]. For example, *Rangelova et al.* [2012] set M at half the total GRACE epoch to separate seasonal and subseasonal variations. However, a large number of lags may lead to misinterpretation of noise, which may be oscillatory if it is Brownian (or correlated) [*Allen and Robertson*, 1996; *Allen and Smith*, 1996]. This may be a problem in Greenland where GRACE meridional stripe noise is superimposed on ice mass signals [*Seo et al.*, 2008].

We use the EEOF filtering method to find EOF patterns using only a few lags [*Plaut and Vautard*, 1994; *von Storch and Navarra*, 1999]. With a few lags, there may be spectral mixing in leading modes, possibly causing annual, subannual, and interannual oscillation and secular variations to contribute to the same mode [*Rangelova et al.*, 2012; *von Storch and Navarra*, 1999]. However, this is not a problem because the goal here is to separate signal from noise. The discussion below shows that signal-dominated modes are easily distinguished from noise-dominated modes by visual inspection of PC/EOFs. Noise-dominated modes show rapid variations in both space and time, while modes dominated by ice mass signals evolve slowly in time.

3. EEOF Filter Development

We examine GRACE estimates of mass change along latitude 70°N through Central Greenland, as shown in Figure 1a. As described earlier, global SH coefficients have been localized to Greenland using a Slepian basis in the SH domain, with a half degree buffer zone extending into the oceans [*Harig and Simons*, 2012]. We use Hovmöller diagrams to show evolution of mass at 70°N latitude over time. In these diagrams, the horizontal axis is east-west distance along 70°N latitude and the vertical axis is time. Figures 1b–1e show Hovmöller diagrams of various estimates of surface mass with time increasing from 2003 (at the bottom) to 2014 (at the top).

Figure 1b is a Hovmöller diagram of GRACE mass variations at 70°N without conventional decorrelation filtering. Figure 1c is a similar Hovmöller diagram after conventional decorrelation filtering. It shows that conventional filtering attenuates signal amplitude and introduces spatial smoothing, which causes signals from east and west coasts to merge. Both Figures 1b and 1c show a gradual change from positive to negative values from 2003 to 2014, indicating steady ice mass loss on both coasts over this period [*Khan et al.*, 2015].

Annual sinusoids and linear trends over time were removed from Figures 1b and 1c, leaving residual variations displayed in Hovmöller diagrams, Figures 1d and 1e. Note that the smaller range of amplitudes requires a different color scale. In Figure 1d, a maximum on the west coast, during the middle years (2006–2010), indicates an accelerated rate of loss superimposed upon the negative trend in Figure 1b. Figure 1d shows that east coast residuals oscillate, with about 2 cycles in 14 years. Both types of temporal variation in the

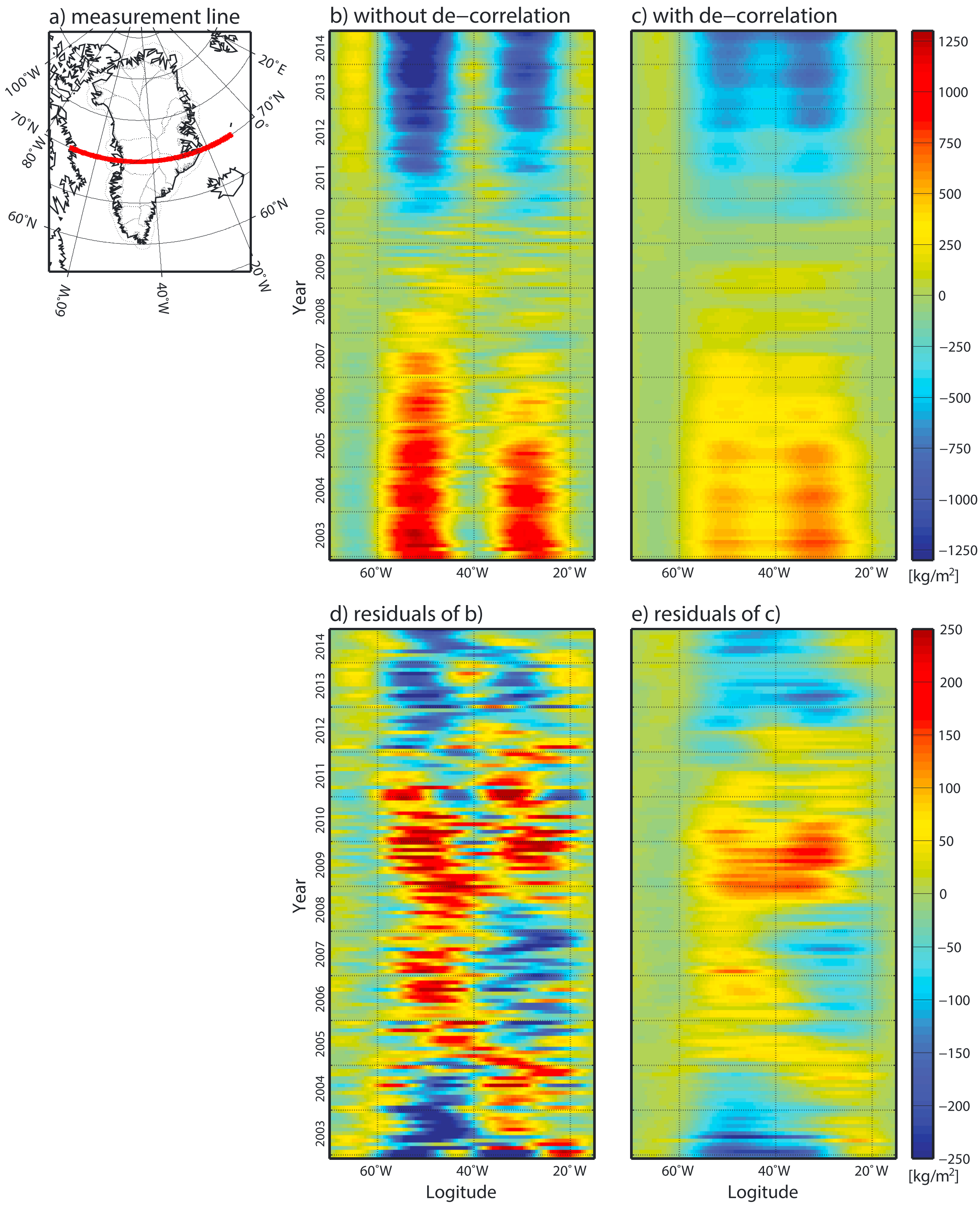

Figure 1. Hovmöller diagrams of ice mass variations for filtered and unfiltered GRACE data along 70°N. (a) Location of the measurement latitude. Diagrams (b) with and (c) without a conventional decorrelation filter. (d and e) Residual diagrams after removing linear trend and seasonal variations.

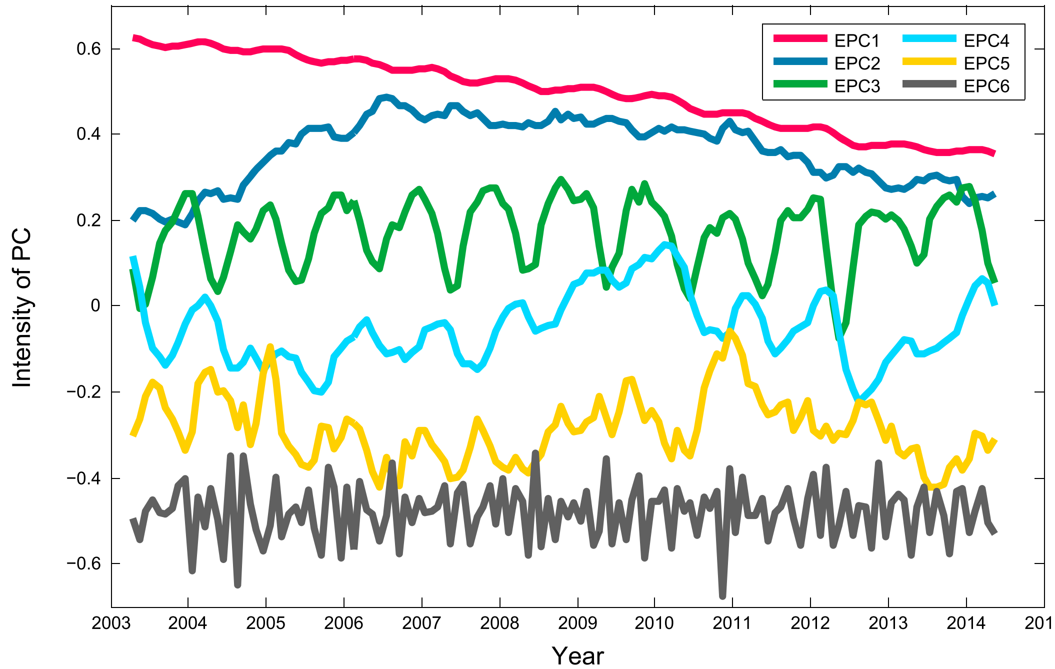

Figure 2. Temporal mode time series from EPC1 to EPC6, which are from $\boldsymbol{u}_1$ to $\boldsymbol{u}_6$ in equation (7). Each curve has a mean of zero, but curves are offset for clarity.

residuals (acceleration in the west and oscillation in the east) are likely caused by SMB fluctuations [*Seo et al.*, 2015]. Residuals of conventionally filtered GRACE data (Figure 1e) are spatially smooth, making it difficult to distinguish east and west coast differences. In Figure 1e it is also difficult to see the high temporal frequency (month-to-month) variations evident in Figure 1d. These high-frequency variations are assumed to be noise that we will remove using EEOF filtering.

We apply the EEOF filter using a window length (*M*) of 5 months, chosen because we expect that noise is unlikely to be correlated beyond 5 months. Figure 2 shows time series of the first six modes ($\boldsymbol{u}_k$ in equation (7), hereafter referred as to EPC*k*). Time series of the first five modes are relatively smooth, evidence that they are dominated by ice mass variations. Modes EPC1 and EPC2 display well-recognized trend and acceleration signals [*Velicogna*, 2009]. Annual, interannual, and possibly subseasonal signals are evident in EPC3 to EPC5. In contrast, EPC6 has the appearance of white noise, with similar behavior for all higher modes. This indicates that EEOF filtering should retain only the first five modes. A similar conclusion comes from analysis of spatial modes (SH coefficients) in Figure 3, which shows panels similar in concept to Hovmöller diagrams, but in which the horizontal coordinate is SH degree and the vertical coordinate is temporal lag. Left and right parts of the panels, respectively, display sine and cosine coefficients separately as they vary over SH degree. We refer to panels in Figure 3 as Hovmöller diagrams, although they are of a novel kind.

Figures 3a–3c display SH order 14 coefficients as they vary over SH degree from 14 to 60, with temporal lag ranging from 0 to 4 months, top to bottom. Order 14 is chosen because it is approximately the GRACE resonance order at which alias error tends to be strongest. Figure 3 shows results for EEOF spatial modes ($\mathbf{V}_k$, $k = 1$, 3, and 6). Figures 3a and 3b (modes 1 and 3) show slow variations with increasing lag. Mode 2 is similar and not shown. The first two modes account for 94.6% of variance, and thus, most ice mass changes in fixed locations such as glacial outlets and coastal areas. Figure 3b shows continuity of correlations with increasing lag, possibly related to ice mass signals at seasonal or shorter time scales undergoing spatial migration (modes 3–5, accounting for 1.8% of variance). In contrast, mode 6 (Figure 3c) shows no organized patterns with changing lag. This would be expected if this mode is noise dominated. The total variance accounted for by noise-dominated modes (6 and higher) is 3.6%, nearly double that of modes 3–5.

GRACE observations filtered using the EEOF method to retain modes 1–5 are displayed in Figure 4. Figure 4a is equivalent to Figure 1c, but with EEOF replacing conventional decorrelation filtering. The steady decline in

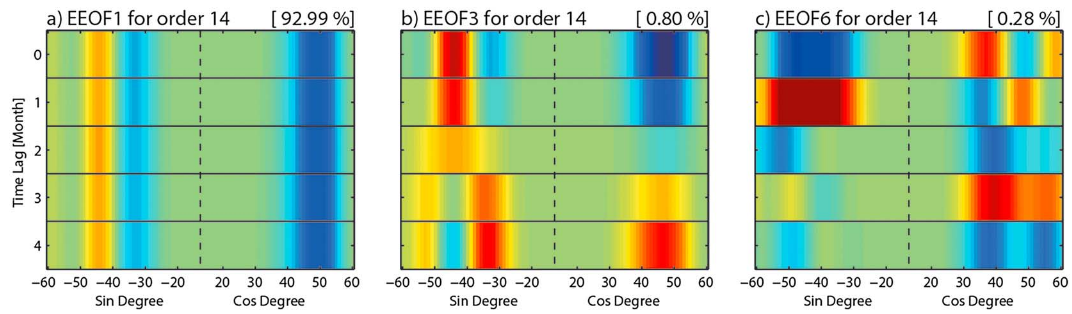

Figure 3. Hovmöller diagrams of different spatial modes for SH coefficients at order 14. Each diagram represents distinct patterns with increasing lag: (a) time-invariant coefficients in the first mode, (b) a mode whose coefficients vary slowly, persisting 2 months or longer, and (c) a mode with random variations with lag, distinctly different from Figures 3a and 3b.

mass over time is evident on both coasts, but separation of east and west coast signals is improved relative to Figure 1c, and there is less attenuation of signal amplitude. After linear trends and annual sinusoids are removed from Figure 4a, residuals in Figure 4b show evidence of mass loss acceleration in the west and oscillations in the east, similar to Figure 1d, but without the high temporal frequency variations due to noise. There is much better separation of east and west coast signals relative to Figure 1e and, again, less amplitude attenuation.

4. GRACE Mass Change Estimates

We compute GRACE mass change time series for the entire GrIS using the three different methods (unfiltered, conventional decorrelation filtered, and EEOF filtered), with results shown in Figure 5. Least squares linear trends are displayed for each method. Slepian-localized SH coefficients are used, without forward modeling [e.g., *Chen et al.*, 2013], with a half degree buffer to correct for signal leakage into the surrounding oceans. The most striking difference in Figure 5 is that the linear trend of the conventionally filtered (gray) time series has a much smaller magnitude than unfiltered and EEOF series (blue and red, respectively), by about 20%. This shows that conventional filtering has significantly attenuated signals along east and west coasts. The unfiltered (blue) series has stronger high-frequency variations relative to the conventionally filter series. These are associated with noise, including meridional stripe noise. These high-frequency changes persist in the conventionally filtered (gray) series, indicating incomplete removal of noise. The EEOF-filtered series (red) shows a trend and seasonal behavior very similar to the unfiltered (blue) line, but with greatly reduced high-frequency variations. Similar differences among unfiltered, conventionally filtered, and EEOF-filtered series were seen in the Hovmöller diagrams. These convincingly demonstrate the effectiveness of the EEOF filter.

We use SMB fields from a regional Greenland climate model, RACMO2.3/GR [*Noël et al.*, 2015], to obtain an independent estimate of ice mass variations within the GrIS in order to compare it with the three GRACE estimates. RACMO2.3/GR provides SMB components including precipitation, evaporation, sublimation, runoff and melted/refrozen water, forced by the European Centre for Medium-Range Weather Forecasts operational forecast analyses. Previous studies have demonstrated that these SMB fields agree well with GrIS mass changes observed by GRACE after including ice discharge estimates [*van den Broeke et al.*, 2009; *van Angelen et al.*, 2014; *McMillan et al.*, 2016; *Xu et al.*, 2016]. *Sasgen et al.* [2012] also confirmed this agreement using satellite altimetry data.

Since the spatial resolution of RACMO2.3/GR is much higher (~11 km) than that of GRACE, monthly SMB fields are resampled to have spatial resolution equivalent to SH degree and order 60. These smoothed SMB fields $\boldsymbol{S}(\boldsymbol{r}_l, t)$ are used to represent change in ice mass over the GRACE era, $\boldsymbol{M}(\boldsymbol{r}_l, t)$:

$$\delta \boldsymbol{M}(\boldsymbol{r}_l, t) = \int_{t_0}^{t} [\boldsymbol{S}(\boldsymbol{r}_l, t) - \boldsymbol{D}(\boldsymbol{r}_l, t)]\mathrm{d}t = \int_{t_0}^{t} [\boldsymbol{S}(\boldsymbol{r}_l, t) - \delta \boldsymbol{D}(\boldsymbol{r}_l, t)]\mathrm{d}t - \boldsymbol{D}_0(\boldsymbol{r}_l)[t - t_0], \quad (10)$$

in which $\boldsymbol{D}(\boldsymbol{r}_l, t)$ is lateral ice flow including ice discharge into the oceans, $\boldsymbol{r}_l$ is a two-dimensional vector with longitude and latitude over Greenland, and t_0 is reference time of January 2003. $\delta \boldsymbol{D}$ is an ice flow divergence anomaly relative to $\boldsymbol{D}_0$, the mean of $\boldsymbol{D}$ (i.e., $\delta \boldsymbol{D} = \boldsymbol{D} - \boldsymbol{D}_0$).

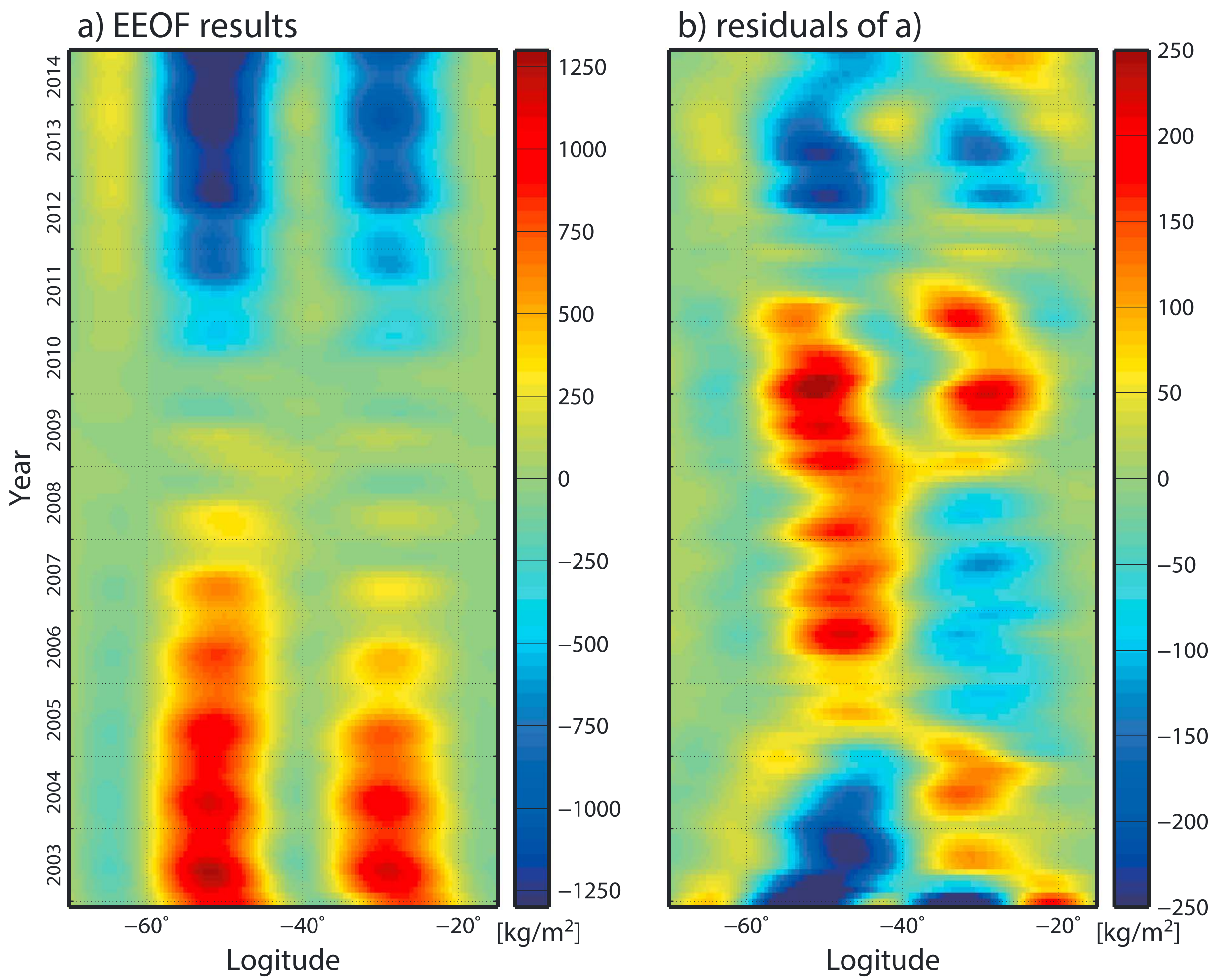

Figure 4. (a) Similar to the Hovmöller diagram in Figure 1c except that EEOF filtering (retaining modes 1–5) replaces conventional decorrelation filtering. (b) Residuals after removing linear trend and seasonal terms from Figure 4a, to be compared with Figure 1e. EEOF filtering greatly improves separation of east and west coast signals, with related clarity of acceleration behavior in the west and interannual variation in the east.

$\boldsymbol{D}_0$ in equation (10) indicates an average field of ice mass change induced by ice flow and can be estimated simply by integration of equation (10) during the whole study period.

$$\boldsymbol{D}_0(\boldsymbol{r}_l) = \left[\delta\boldsymbol{M}(\boldsymbol{r}_l, t_e) - \int_{t_0}^{t_e}\boldsymbol{S}(\boldsymbol{r}_l, t)\mathrm{d}t\right]/(t_e - t_0), \tag{11}$$

in which t_e is the end month of the study period. Because $\delta\boldsymbol{D}$ in equation (10) is the anomaly, its integrated value is zero. Although the three estimates of ice mass change shown in Figure 5 exhibit some differences in $\delta\boldsymbol{M}$ at seasonal or subseasonal time scales, the mean ice mass loss rates (i.e., $\delta\boldsymbol{M}/t$) are very similar because the dominant negative trends are much stronger than seasonal or subseasonal variations, so we adopt $\delta\boldsymbol{M}/t$ computed from GRACE data without decorrelation filtering applied.

Wintertime ice discharge variations tend to be nearly constant or to show small increases after a seasonal minimum in the fall [*Bartholomew et al.*, 2010; *Joughin et al.*, 2008, 2010; *Rignot and Kanagaratnam*, 2006]. Thus, the contribution of $\delta\boldsymbol{D}$ during winter months should be small relative to other seasons, and month-to-month ice mass variations ought to be dominated by SMB and the mean discharge $\boldsymbol{D}_0$, so that

$$\delta\boldsymbol{M}_{t_1}^{t_2} \equiv \delta\boldsymbol{M}(\boldsymbol{r}_l, t_2) - \delta\boldsymbol{M}(\boldsymbol{r}_l, t_1) = \int_{t_1}^{t_2}\boldsymbol{S}\mathrm{d}t - (t_2 - t_1)\boldsymbol{D}_0, \tag{12}$$

where t_1 and t_2 are two successive months (i.e., $t_2 - t_1$=1) and the right-hand integral term is approximated by the average SMB, $[\boldsymbol{S}(\boldsymbol{r}_l, t_1) + \boldsymbol{S}(\boldsymbol{r}_l, t_2)]/2$. With equation (12), we can compare monthly difference mass variations observed by GRACE with the SMB derived by RACMO2.3/GR during winter seasons.

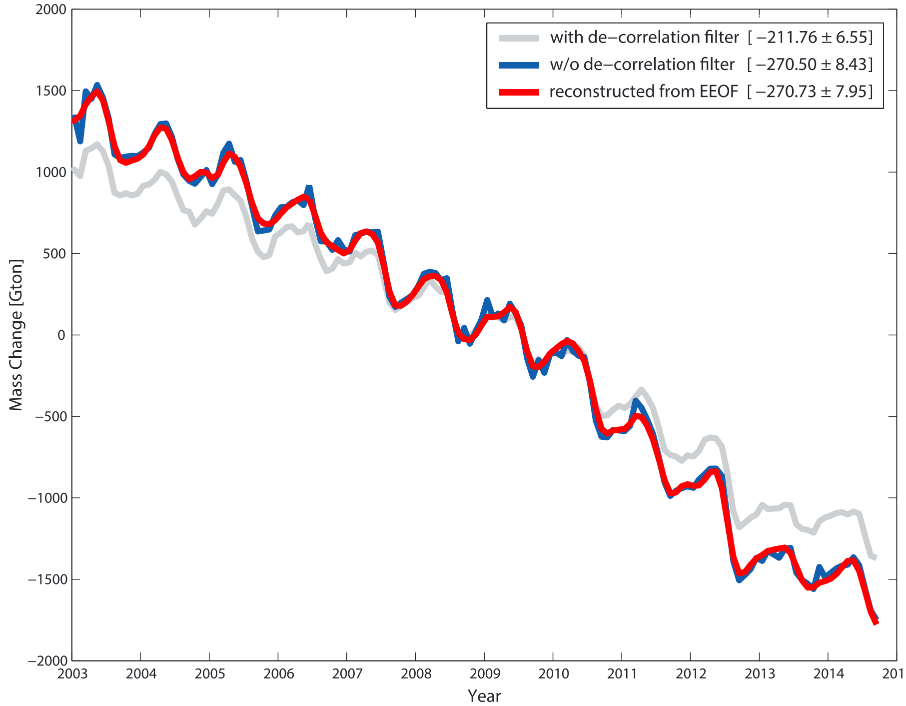

Figure 5. GrIS mass variations with (gray) and without (blue) decorrelation filtering and with EEOF filtering (red). Linear trend estimates for each time series with 95% confidence intervals in units of gigaton per year. All clearly show seasonal variations but different trends and relative sizes of short period variations.

Figure 6 shows RACMO2.3/GR (SMB) and GRACE ($\delta \boldsymbol{M}_{t_1}^{t_2}$) compared using equation (12). Figures 6a–6c show estimated $\delta \boldsymbol{M}_{t_1}^{t_2}$ derived from SMB and $\boldsymbol{D}_0$ during adjacent months spanning October 2008 to January 2009. There is strong positive SMB in southern basins during October–December 2008, with reduced magnitude from December 2008 to January 2009. Figures 6d–6f show GRACE estimate (no decorrelation filtering) of ($\delta \boldsymbol{M}_{t_1}^{t_2}$). The GRACE results show meridional stripes (correlated noise) and large differences relative to (SMB-$\boldsymbol{D}_0$) (note a difference in scales relative to Figures 6a–6c). Figures 6g–6i show GRACE estimates after applying the conventional decorrelation filter. In southern regions, results are similar to estimates from SMB-$\boldsymbol{D}_0$ (Figures 6a–6c), but there are artifacts in the GRACE results in the north that are absent in SMB-$\boldsymbol{D}_0$ results. Finally, Figures 6j–6l show GRACE estimates filtered by the EEOF method. They are very similar to Figures 6a–6c (from SMB-$\boldsymbol{D}_0$). We interpret small differences as due to wintertime contributions of $\delta \boldsymbol{D}$ which was neglected.

GRACE mass concentration (mascon) solutions [e.g., *Save et al.*, 2016] are gridded surface mass change fields which lack correlated errors (meridional stripes) that afflict GRACE SH solutions. In the supporting information, we analyze mascon solutions in a manner similar to that above and find them to be relatively limited in their ability to study regional-scale and subseasonal ice mass change over the GrIS.

Given the demonstration above that EEOF filtering is effective in suppressing correlated error while preserving ice mass signal, we now examine seasonal average month-to-month GrIS ice mass changes. Figure 7 shows EEOF-filtered GRACE estimates of mean differences in ice mass between adjacent months over the study period, 2004 to 2013. In winter (November to March), ice mass accumulation is evident in the south. Both fall and spring show relatively small changes, while summer months (June to September) show large losses, especially in the south. In particular, difference maps during the summer show large losses at major glacial outlets such as Helheim and Kangerdlugssuaq on the west coast and Jakobshavn Isbræ on the east [*Howat et al.*, 2011; *Joughin et al.*, 2010]. A likely explanation is enhanced discharge associated with meltwater effects at marine-terminating glaciers [*Schoof*, 2010]. Note that high-altitude inland regions show accumulation during the summer.

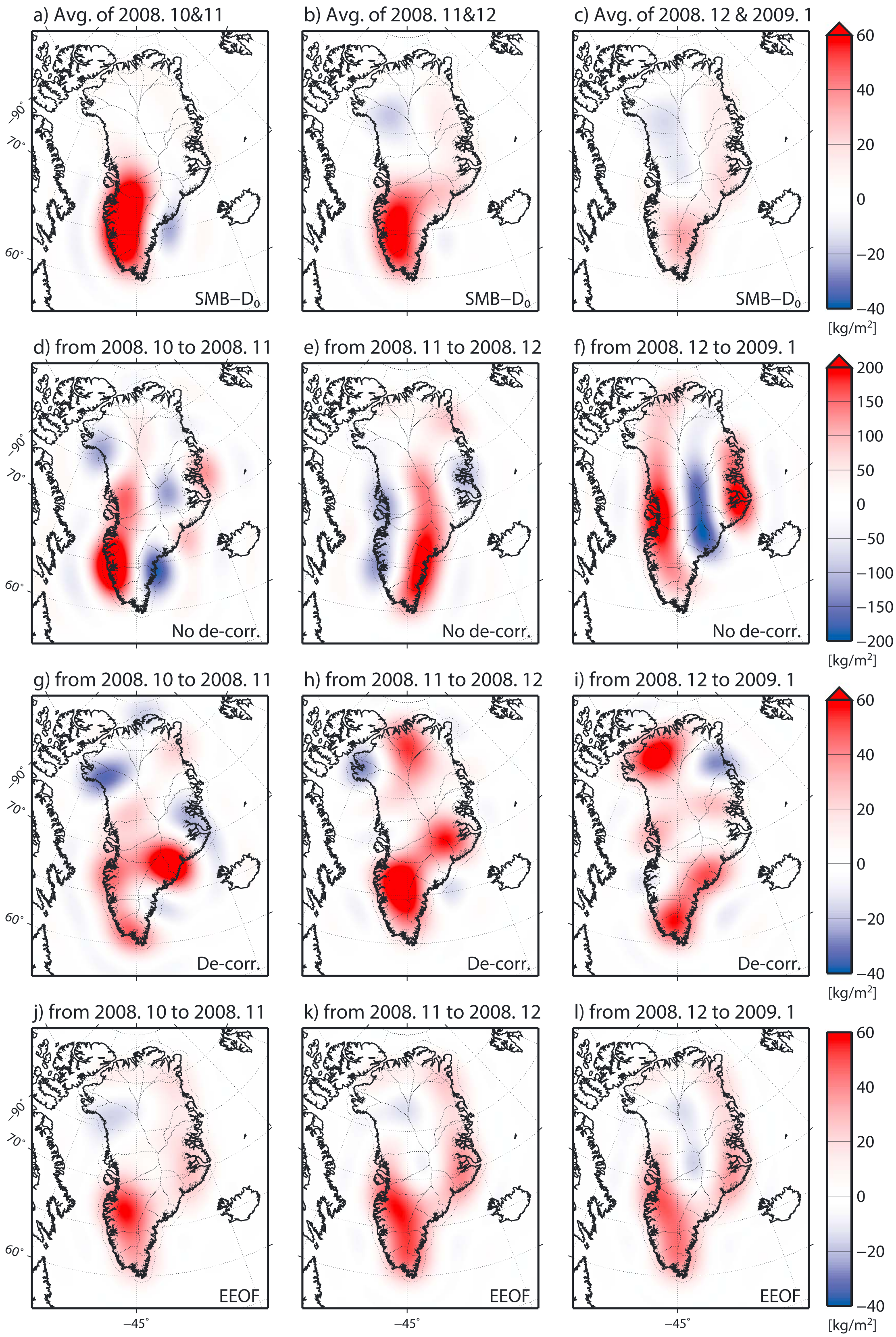

Figure 6. Comparison of SMB fields (a–c) calculated by RACMO2.3/GR after removing reference ice discharge field, $\boldsymbol{D}_0$, and (d–f) consecutive month-to-month GRACE ice mass variation maps without filtering, with (g–i) conventional decorrelation filtering and (j–l) using EEOF filtering.

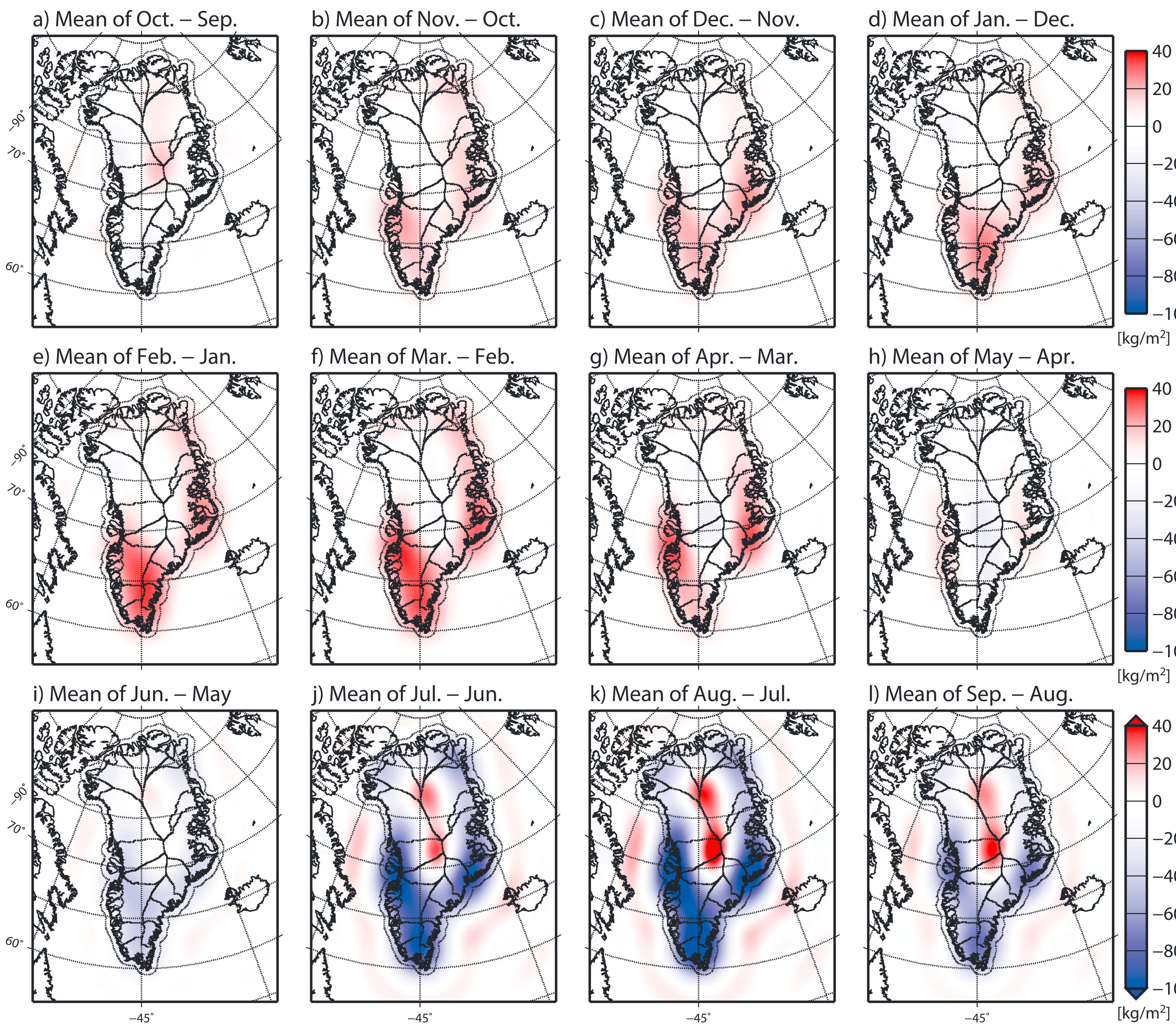

Figure 7. Mean monthly difference maps of ice mass from 2004 to 2013, calculated by averaging of $\delta M_{t_1}^{t_2}$s from EEOF-filtered data for the study period.

5. Conclusions

GRACE SH time-varying mass fields are corrupted by north-south (meridional) stripes due to aliasing of high-frequency signals such as atmospheric and ocean bottom mass redistribution. This correlated stripe noise contaminates high degree and order SH coefficients. A conventional decorrelation filter has been used in many studies to remove these stripes. Although effective, the conventional method may also attenuate or smooth the signal, and there is evidence in Figures 6g–6i that it is not able to suppress high-frequency noise. These problems are particularly important with regard to GRACE estimates over the GrIS, because there the signal has a dominant north-south orientation along Greenland's coastline.

The EEOF method decomposes monthly GRACE data into spatial and temporal modes and provides results relatively free of correlated noise by retaining only those modes that change slowly over several months. The EEOF method is more effective than conventional decorrelation filtering, improving estimates of mass change for the entire continent and allowing resolution of changes at finer temporal and spatial scales, as demonstrated by comparison with regional climate model estimates.

EEOF filtering provides sensible estimates of seasonal and subseasonal mass change over the GrIS, which have been difficult to obtain with conventional decorrelation filtering. EEOF-filtered estimates show significant ice mass losses at major glacial outlets and other locations, demonstrating that they are suitable for studies at relatively fine spatial and temporal resolution. In combination with in situ and model data, EEOF-filtered results should allow further understanding of seasonal and longer-term changes in ice discharge and ice dynamics.

Acknowledgments

This study was supported by Korea Polar Research Institute (KOPRI) research grant PM16020 and Korea Meteorological Industry Promotion Agency (KMIPA) research grant KMIPA2015-3033. GRACE monthly solutions, degree 1 and 2 SH coefficients, and the PGR model are available at ftp://podaac.jpl.nasa.gov. C. Wilson received support from the Geology Foundation of the University of Texas. RACMO2.3/GR data are available upon request in Institute for Marine and Atmospheric Research, Utrecht University (https://www.projects.science.uu.nl/iceclimate/models/greenland.php).

References

A, G., J. Wahr, and S. Zhong (2013), Computations of the viscoelastic response of a 3-D compressible Earth to surface loading: An application to glacial isostatic adjustment in Antarctica and Canada, *Geophys. J. Int.*, *192*(2), 557–572, doi:10.1093/gji/ggs030.

Allen, M. R., and A. W. Robertson (1996), Distinguishing modulated oscillations from coloured noise in multivariate datasets, *Clim. Dyn.*, *12*(11), 775–784, doi:10.1007/s003820050142.

Allen, M. R., and L. A. Smith (1996), Monte Calo SSA: Detecting irregular oscillations in the presence of colored noise, *J. Clim.*, *9*(12), 3373–3404, doi:10.1175/1520-0442(1996)009<3373:MCSDIO>2.0.CO;2.

Bartholomew, I., P. Nienow, D. Mair, A. Hubbard, M. A. King, and A. Sole (2010), Seasonal evolution of subglacial drainage and acceleration in a Greenland outlet glacier, *Nat. Geosci.*, *3*(6), 408–411, doi:10.1038/ngeo863.

Boergens, E., E. Rangelova, M. G. Sideris, and J. Kusche (2014), Assessment of the capabilities of the temporal and spatiotemporal ICA method for geophysical signal separation in GRACE data, *J. Geophys. Res. Solid Earth*, *119*, 4429–4447, doi:10.1002/2013JB010452.

Chambers, D. P. (2006), Evaluation of new GRACE time-variable gravity data over the ocean, *Geophys. Res. Lett.*, *33*, L17603, doi:10.1029/2006GL027296.

Chen, J. L., C. R. Wilson, and B. D. Tapley (2013), Contribution of ice sheet and mountain glacier melt to recent sea level rise, *Nat. Geosci.*, *6*(7), 549–552, doi:10.1038/ngeo1829.

Cheng, M., and B. D. Tapley (2004), Variations in the Earth's oblateness during the past 28 years, *J. Geophys. Res.*, *109*, B09402, doi:10.1029/2004JB003028.

Frappart, F., G. Ramillien, P. Maisongrande, and M.-P. Bonnet (2010), Denoising satellite gravity signals by independent component analysis, *IEEE Geosci. Remote Sens. Lett.*, *7*, 421–425, doi:10.1109/LGRS.2009.2037837.

Forootan, E., and J. Kusche (2012), Separation of global time-variable gravity signals into maximally independent components, *J. Geod.*, *86*, 477–497, doi:10.1007/s00190-011-0532-5.

Ghil, M., et al. (2002), Advanced spectral methods for climatic time series, *Rev. Geophys.*, *40*(1), 1003, doi:10.1029/2000RG000092.

Hannachi, A., I. T. Jolliffe, and D. B. Stephenson (2007), Empirical orthogonal functions and related techniques in atmospheric science: A review, *Int. J. Climatol.*, *27*(9), 1119–1152, doi:10.1002/joc.1499.

Harig, C., and F. J. Simons (2012), Mapping Greenland's mass loss in space and time, *PNAS*, *109*(49), 19,934–19,937, doi:10.1073/pnas.1206785109.

Howat, I. M., Y. Ahn, I. Joughin, M. R. van den Broeke, J. T. M. Lenaerts, and B. Smith (2011), Mass balance of Greenland's three largest outlet glaciers, 2000–2010, *Geophys. Res. Lett.*, *38*, L12501, doi:10.1029/2011GL047565.

Joughin, I., S. B. Das, M. A. King, B. E. Smith, I. M. Howat, and T. Moon (2008), Seasonal speedup along the western flank of the Greenland Ice Sheet, *Science*, *320*(5877), 781–783, doi:10.1126/science.1153288.

Joughin, I., B. E. Smith, I. M. Howat, T. Scambos, and T. Moon (2010), Greenland flow variability from ice-sheet-wide velocity mapping, *J. Glaciol.*, *56*(197), 415–430, doi:10.3189/002214310792447734.

Khan, A. S., A. Aschwanden, A. A. Bjørk, J. Wahr, K. K. Kjeldsen, and H. K. Kjær (2015), Greenland ice sheet mass balance: A review, *Rep. Prog. Phys.*, *78*(4), 046801, doi:10.1088/0034-4885/78/4/046081.

Kusche, J. (2007), Approximate decorrelation and non-isotropic smoothing of time-variable GRACE-type gravity field models, *J. Geod.*, *81*, 733–749, doi:10.1007/s00190-007-0143-3.

Moon, T., I. Joughin, B. Smith, M. R. van den Broeke, W. J. van de Berg, B. Noël, and M. Usher (2014), Distinct patterns of seasonal Greenland glacier velocity, *Geophys. Res. Lett.*, *41*, 7209–7216, doi:10.1002/2014GL061836.

McMillan, M., et al. (2016), A high-resolution record of Greenland mass balance, *Geophys. Res. Lett.*, *43*, 7002–7010, doi:10.1002/2016GL069666.

Navarra, A., and V. Simincini (2010), *A Guide to Empirical Orthogonal Functions for Climate Data Analysis*, pp. 87–90, Springer Science & Business Media, Dordrecht, Netherlands, doi:10.1007/978-90-481-3702-2.

Noël, B., W. J. van de Berg, E. van Meijgaard, P. Kuipers Munneke, R. S. W. van de Wal, and M. R. van den Broeke (2015), Evaluation of the updated regional climate model RACMO2.3: Summer snowfall impact on the Greenland Ice Sheet, *Cryosphere*, *9*(5), 1831–1844, doi:10.5194/tc-9-1831-2015.

Plaut, G., and R. Vautard (1994), Spells of low-frequency oscillations and weather regimes in Northern Hemisphere, *J. Atmos. Sci.*, *51*, 210–236, doi:10.1175/1520-0469(1994)051<0210:SOLFOA>2.0.CO;2.

Rangelova, E., W. van der Wal, M. Sideris, and P. Wu (2009), Spatiotemporal analysis of the GRACE-derived mass variations in North America by means of multi-channel singular spectrum analysis, in *IAG Symposia Gravity, Geoid and Earth Observation*, vol. 135, edited by S. Mertikas, pp. 539–546, Springer, Chania, Greece.

Rangelova, E., M. G. Sideris, and J. W. Kim (2012), On the capabilities of the multi-channel singular spectrum method for extracting the main periodic and non-periodic variability from weekly GRACE data, *J. Geodyn.*, *54*, 64–78, doi:10.1016/j.jog.2011.10.006.

Rignot, E., and P. Kanagaratnam (2006), Changes in the velocity structure of the Greenland Ice Sheet, *Science*, *311*(5763), 986–990, doi:10.1126/science.1121381.

Rignot, E., and J. Mouginot (2012), Ice flow in Greenland for the International Polar Year 2008–2009, *Geophys. Res. Lett.*, *39*, L11501, doi:10.1029/2012GL051634.

Rignot, E., I. Velicogna, M. R. van den Broeke, A. Monaghan, and J. Lenaerts (2011), Acceleration of the contribution of the Greenland and Antarctic ice sheets to sea level rise, *Geophys. Res. Lett.*, *38*, L05503, doi:10.1029/2011GL046583.

Sasgen, I., M. R. van den Broeke, J. L. Bamber, E. Rignot, L. S. Sørensen, B. Wouters, Z. Martinec, I. Velicogna, and S. B. Simonsen (2012), Timing and origin of recent regional ice-mass loss in Greenland, *Earth Planet. Sci. Lett.*, *333-334*, 293–303, doi:10.1016/j.epsl.2012.03.033.
Save, H., S. Bettadpur, and B. D. Tapley (2016), High-resolution CSR GRACE RL05 mascons, *J. Geophys. Res. Solid Earth*, *121*, 7547–7569, doi:10.1002/2016JB013007.
Schoof, C. (2010), Ice-sheet acceleration driven by melt supply variability, *Nature*, *468*(7325), 803–806, doi:10.1038/nature09618.
Schmeer, M., M. Schmidt, W. Bosch, and F. Seitz (2012), Separation of mass signals within GRACE monthly gravity field models by means of empirical orthogonal functions, *J. Geod.*, *59–60*, 124–132, doi:10.1016/j.jog.2012.03.001.
Schrama, E. J. O., and B. Wouters (2011), Revisiting Greenland ice sheet mass loss observed by GRACE, *J. Geophys. Res.*, *116*, B02407, doi:10.1029/2009JB006847.
Schrama, E. J. O., B. Wouters, and D. A. LavallÈe (2007), Signal and noise in Gravity Recovery and Climate Experiment (GRACE) observed surface mass variations, *J. Geophys. Res.*, *112*, B08407, doi:10.1029/2006JB004882.
Schrama, E. J. O., B. Wouters, and R. Rietbroek (2014), A mascon approach to assess ice sheet and glacier mass balances and their uncertainties from GRACE data, *J. Geophys. Res. Solid Earth*, *119*, 6048–6066, doi:10.1029/2013JB010923.
Seo, K.-W., C. R. Wilson, J. Chen, and D. E. Waliser (2008), GRACE's spatial aliasing error, *Geophys. J. Int.*, *172*(1), 41–48, doi:10.1111/j.1365-246x.2007.03611.x.
Seo, K.-W., D. E. Waliser, C.-K. Lee, B. Tian, T. Scambos, B.-M. Kim, J. H. van Angelen, and M. R. van den Broeke (2015), Accelerated mass loss from Greenland ice sheet: Links to atmospheric circulation in the North Atlantic, *Global Planet. Change*, *128*, 61–71, doi:10.1016/j.gloplacha.2015.02.006.
Slepian, D. (1983), Some comments on Fourier analysis, uncertainty and modeling, *SIAM Rev.*, *25*(3), 379–393, doi:10.1137/1025078.
Swenson, S., and J. Wahr (2006), Post-processing removal of correlated errors in GRACE data, *Geophys. Res. Lett.*, *33*, L08402, doi:10.1029/2005GL025285.
Swenson, S., D. Chambers, and J. Wahr (2008), Estimating geocenter variations from a combination of GRACE and ocean model output, *J. Geophys. Res.*, *113*, B08410, doi:10.1029/2007JB005338.
Tangang, F. T., B. Tang, A. H. Monahan, and W. W. Hsieh (1998), Forecasting ENSO events: A neural network–extended EOF approach, *J. Clim.*, *11*(1), 29–41, doi:10.1175/1520-0442(1998)011<0029:FEEANN>2.0.CO;2.
van Angelen, J. H., M. R. van den Broeke, B. Wouters, and J. T. M. Lenaerts (2014), Contemporary (1960–2012) evolution of the climate and surface mass balance of the Greenland Ice Sheet, *Surv. Geophys.*, *35*(5), 1155–1174, doi:10.1007/s10712-013-9261-z.
van den Broeke, M., J. Bamber, J. Ettema, E. Rignot, E. Schrama, W. J. van de Berg, E. van Meijgaard, I. Velicogna, and B. Wouters (2009), Partitioning recent Greenland mass loss, *Science*, *326*(5955), 984–986, doi:10.1126/science.1178176.
Vaughan, D. G., et al. (2013), Observations: Cryosphere, in *Climate Change 2013: Physical Science Basis. Contribution of Working Group I to the Fifth Assessment Report of the Intergovernmental Panel on Climate Change*, edited by T. F. Stocker et al., Cambridge Univ. Press, Cambridge, U. K.
Velicogna, I. (2009), Increasing rates of ice mass loss from the Greenland and Antarctic ice sheets revealed by GRACE, *Geophys. Res. Lett.*, *36*, L19503, doi:10.1029/2009GL040222.
Velicogna, I., and J. Wahr (2013), Time-variable gravity observations of ice sheet mass balance: Precision and limitations of the GRACE satellite data, *Geophys. Res. Lett.*, *40*, 3055–3063, doi:10.1002/grl50527.
Vianna, M. L., V. V. Menezes, and D. P. Chambers (2007), A high resolution satellite-only GRACE-based mean dynamic topography of the South Atlantic Ocean, *Geophys. Res. Lett.*, *34*, L24604, doi:10.1029/2007GL031912.
von Storch, H., and A. Navarra (1999), *Analysis of Climate Variability: Applications of Statistical Techniques*, pp. 259–280, Springer, Berlin, doi:10.1007/978-3-662-03167-4.
Wahr, J., M. Molenaar, and F. Bryan (1998), Time variability of the Earth's gravity field: Hydrological and oceanic effects and their possible detection using GRACE, *J. Geophys. Res.*, *103*(B12), 30,205–30,229, doi:10.1029/98JB02844.
Weare, B. C., and J. S. Nasstrom (1982), Examples of extended empirical orthogonal function analyses, *Mon. Weather Rev.*, *110*(6), 481–485, doi:10.1175/1520-0493(1982)110<0481:EOEEOF>2.0.CO;2.
Wieczorek, M. A., and F. J. Simons (2005), Localized spectral analysis on the sphere, *Geophys. J. Int.*, *162*(3), 655–675, doi:10.1111/j.1365-246X.2005.02687.x.
Wouters, B., and E. J. O. Schrama (2007), Improved accuracy of GRACE gravity solutions through empirical orthogonal function filtering of spherical harmonics, *Geophys. Res. Lett.*, *34*, L23711, doi:10.1029/2007gl032098.
Wouters, B., D. Chambers, and E. J. O. Schrama (2008), GRACE observes small-scale mass loss in Greenland, *Geophys. Res. Lett.*, *35*, L20501, doi:10.1029/2008GL034816.
Wouters, B., J. L. Bamber, M. R. van den Broeke, J. T. M. Lenaerts, and I. Sasgen (2013), Limits in detecting acceleration of ice sheet mass loss due to climate variability, *Nat. Geosci.*, *6*(8), 613–616, doi:10.1038/ngeo1874.
Xu, Z., E. J. O. Schrama, W. van der Wal, M. R. van den Broeke, and E. M. Enderlin (2016), Improved GRACE regional mass balance estimates of the Greenland ice sheet cross-validated with the input-output method, *Cryosphere*, *10*(2), 895–912, doi:10.5194/tc-10-895-2016.
Zwally, H. J., et al. (2011), Greenland ice sheet mass balance: Distribution of increased mass loss with climate warming; 2003–07 versus 1992–2002, *J. Glaciol.*, *57*(201), 88–102, doi:10.3189/002214311795306682.
Zotov, L. V., C. K. Shum, and N. L. Frolova (2015), Gravity changes over Russian river basins from GRACE, in *Planetary Exploration and Science: Recent Results and Advances*, edited by S. Jin, N. Haghighipour and W.-H. Ip, pp. 45–59, Springer, Berlin, Heidelberg, doi:10.1007/978-3-662-45052-9_3.
Zotov, L., C. Bizouard, and C. K. Shum (2016), A possible interrelation between Earth rotation and climatic variability at decadal time-scale, *Geod. Geodynam.*, *7*(3), 216–222, doi:10.1016/j.geog.2016.05.005.